Dalton Transactions

RSC Publishing

PAPER

View Article Online
View Journal | View Issue



Cite this: *Dalton Trans.*, 2013, **42**, 11411

# Solvothermal synthesis of antimony sulfide dendrites for electrochemical detection of dopamine

Wenguang Tao,[a] Jianling Wang,[b] Dapeng Wu,[a,c] Jiuli Chang,[a,c] Feng Wang,[a] Zhiyong Gao,*[a] Fang Xu[a,c] and Kai Jiang*[a,c]

Received 2nd June 2013,
Accepted 6th June 2013

DOI: 10.1039/c3dt51439k

www.rsc.org/dalton

$Sb_2S_3$ dendrites composed of 1-dimensional rods were prepared by a facile solvothermal reaction. The dosage of the poly(acrylic acid) (PAA) morphology-controlling reagent and the reaction temperature are key factors determining the final morphology of the product. Temporal experiments revealed that the formation of $Sb_2S_3$ dendrites experienced successive stages including precipitate reaction, crystallization and tip splitting. The as-prepared $Sb_2S_3$ dendrites were further employed as sensing material for electrochemical detection of dopamine (DA). A cyclic voltammogram (CV) showed that an $Sb_2S_3$ dendrite modified electrode enables the selective electro-oxidation of DA in the presence of ascorbic acid (AA). The constructed biosensor demonstrated a linear response range of 0.125–160 μM and a detection limit of 0.1 μM, which suggests that the $Sb_2S_3$ dendrites are promising sensing materials in the electrochemical analysis of DA.

## Introduction

Antimony sulfide ($Sb_2S_3$) is a versatile semiconducting material possessing superior optical, photoelectrical and electrochemical properties; it can be potentially applied in optical materials,[1] sensitizers of photovoltaic devices,[2] photocatalysts[3] as well as electrode materials in nickel–metal hydride batteries and lithium ion batteries.[4] The crystallized $Sb_2S_3$ generally adopts an orthorhombic anisotropic structure in the form of 1-dimensional nanowires or nanorods, which could further offer outstanding nonlinear current–voltage characteristics,[5] and ferroelectric and piezoelectric behaviors.[6] Given the abundant application performance of $Sb_2S_3$ and the morphology or crystallinity dependent properties of nanomaterials, $Sb_2S_3$ materials with various morphologies, *e.g.* microspheres,[4a] nanorings,[7] 1-dimensional nanowires, nanorods[5–8] and assembled or split 3-dimensional architectures, were designed to expand the application performances.[1b,9] Moreover, the understanding of the formation mechanism of these materials can offer valuable guidance on adopting suitable strategies to elaborately tailor $Sb_2S_3$ materials with desired shapes and therefore performances.

The intermediate valence of Sb(III) in $Sb_2S_3$ implies that it should possess certain catalytic properties, for the redox conversion between different valences of catalysts is accepted as the main catalyzing mechanism for certain reactions. Additionally, the low solubility product constant of $Sb_2S_3$ ($1.5 \times 10^{-93}$) hinders its dissolution in aqueous solution.[3b] Moreover, the high crystallinity, special shape and superficial atoms bonding mode of $Sb_2S_3$ are also essential for the surface-related catalytic reaction. All of these factors are favorable for the application of $Sb_2S_3$ as catalysts for certain reactions or electrode materials in electrochemical batteries.[4] The application of $Sb_2S_3$ as sensing materials for the detection of electrochemically active substances is also expectable, but as far as we know, few reports involved the application of $Sb_2S_3$ in the sensing of electroactive molecules. The investigation of this field is beneficial for further exploiting the potential of $Sb_2S_3$ materials.

Dopamine (DA) is an important biomolecule that widely exists in the brain which acts as a neurotransmitter for message transfer in the central nervous system.[10] An abnormally low DA concentration is the culprit for some neurological disorders such as schizophrenia, Huntington's disease and Parkinson's syndrome,[11] which are among the most serious health issues disturbing human kind. Therefore, it is imperative to develop simple, rapid and efficient quantitative DA determination methods so that the diagnosis, cure and prevention of these diseases can be achieved. Apart from the traditional methods such as spectrophotometry, chromatography and coupled liquid chromatography–mass spectrometry for quantitative DA analysis,[12] the electrochemical technique is also promising for DA detection due to its activity in electrochemical oxidation. The DA sample detection can be rapidly and sensitively performed on an electrochemical instrument

[a]*School of Chemistry and Chemical Engineering, Henan Normal University, Henan Xinxiang 453007, P.R. China. E-mail: zygao512@163.com; Tel: +86373 3326336*
[b]*Department of Quality Detection and Management, Zhengzhou College of Animal and Husbandry Engineering, Henan Zhengzhou, 450008, China*
[c]*Collaborative Innovation Center of Motive Power & Key Materials, Henan, 453007, P.R. China. E-mail: jiangkai6898@126.com; Tel: +86373 3326209*

with low cost. However, the coexistence of electroactive AA in practical bio-samples often interferes with the electrochemical response of DA owing to the similar oxidation potential. Sensing materials with exclusive electrocatalytic activity on DA or different electrochemical response potentials between DA and AA can overcome this problem. Therefore, different types of sensing materials including carbon or doped carbon materials,[13] semiconductors,[14] functionalized graphene or carbon nanotubes[15] and polymers[16] were developed to selectively detect DA in the presence of AA. Compared with the aforementioned sensing materials, the studies on the sensing ability of sulfides in DA detection remain rarely reported; it is essential to explore the performance of sulfides in the sensing of electroactive molecules.

Herein, $Sb_2S_3$ dendrites were synthesized by a facile solvothermal reaction using PAA as a morphology-controlling reagent. The formation of the dendrites includes the precipitate reaction toward amorphous $Sb_2S_3$ spheres, the ripening and crystallization to aggregated rods and the following tip splitting process. Used as a sensing material for selective electro-oxidation of DA, the $Sb_2S_3$ dendrites demonstrated an acceptable detection limit, a wide linear response range and good selectivity, highlighting the potential in electrochemical DA sensing.

## Experimental

### Reagents

$SbCl_3$, thiourea and ethylene glycol (EG) were purchased from Shanghai Chemical Reagent Co. Ltd. PAA ($M_w$ = 800–1000), potassium dihydrogen phosphate ($KH_2PO_4$) and dipotassium hydrogen phosphate ($K_2HPO_4$) were purchased from Tianjin Deen Reagent Company. DA and AA were purchased from Aladdin Reagent Corporation. All the reagents were used as received without further purification. Phosphate buffer solution (PBS, pH 6) was prepared by dissolving $K_2HPO_4$ and $KH_2PO_4$ in double distilled water for electrochemical tests.

### Synthesis of $Sb_2S_3$ dendrites

In a typical synthesis of $Sb_2S_3$ dendrites, 0.5 mL of PAA, 0.114 g (0.5 mmol) of antimony chloride ($SbCl_3$) and 0.114 g (1.5 mmol) of thiourea were dissolved in 35 mL EG under magnetic stirring to form a homogeneous solution. The solution was then sealed into a Teflon-lined autoclave with a capacity of 40 mL and heated at 160 °C for 12 h. After being cooled to room temperature naturally, the afforded black precipitate was centrifuged and washed repeatedly with ethanol and distilled water and then vacuum dried at 60 °C. To monitor the formation process toward $Sb_2S_3$ dendrites, the autoclave was taken out at different time intervals and cooled rapidly with a water bath to terminate the reaction, the intermediate products were collected to investigate the morphology evolution. Controlled trials by varying of PAA dosage and solvothermal temperature were also carried out to clarify the influence of reaction conditions.

### Characterization

The resulting products were characterized by X-ray diffraction (XRD, a Bruker Advance-D8 power diffractometer with Cu Kα radiation, $\lambda$ = 0.154178 nm at 40 kV and 100 mA flux), scanning electron microscopy (SEM, JEOL JSM-6390LV) and high-resolution transmission electron microscopy (HRTEM, JEOL JEM-2100).

### Fabrication of the $Sb_2S_3$ dendrites modified electrode

Glassy carbon electrode (GCE $d$ = 3 mm) was firstly polished with alumina slurry to form a mirror-like surface, rinsed repeatedly with distilled water, then ultrasonicated successively in nitric acid (1 : 1), anhydrous ethanol and double distilled water (each for 5 min) and dried at room temperature. To fabricate a modified electrode, 4 mg $Sb_2S_3$ dendrites and a 5 μL Nafion ethanol solution (0.5%) were ultrasonically dispersed in a 1 mL ethanol solvent. Then, 20 μL of the dispersion (4 mg $mL^{-1}$) was dropped onto the clean GCE and dried in air for DA detection.

### Electrochemical measurement

The electrochemical measurements were performed on a CHI 660D workstation (Shanghai Chenhua instruments, China). A conventional three-electrode system, including a $Sb_2S_3$ modified GCE or blank GCE as a working electrode, a Ag/AgCl reference electrode and a platinum wire counter electrode, was used in the measurements. Freshly prepared analytes dissolved in pH 6 PBS were used in all the electrochemical measurements. The current response at different electrodes, the effect of scan rate and the interference of AA on DA detection were recorded using CV. The response currents at different DA concentrations were measured using differential pulse voltammetry (DPV).

## Results and discussion

### Morphologies and structures

The XRD pattern of the yielded black $Sb_2S_3$ powder is shown in Fig. 1. The narrow and strong diffraction peaks indicate the high crystallinity of the product, and all the peaks can be well indexed to orthorhombic phase $Sb_2S_3$ (JCPDS 42-1393). No peaks belonging to other phases or impurities can be discerned, evidencing the high purity of the product.

The morphological and structural features of the as-synthesized products were characterized by SEM and HRTEM. As shown in Fig. 2a, the product exhibits broom-like dendrites composed of bundles of 1-dimensional rods with diameters of 200–600 nm and lengths of 5–15 μm; each bundle of the radially arranged rods share a common root. SEM with higher magnification (Fig. 2b) reveals that the primary rods are prisms with high aspect ratios. The TEM image shown in Fig. 2c evidences the solid interior of the primary prism. The HRTEM image (Fig. 2d) magnified from the tip of the prism (black box in Fig. 2c) demonstrates clear lattice fringes, evidencing the high crystallinity of the product. The lattice fringes

 

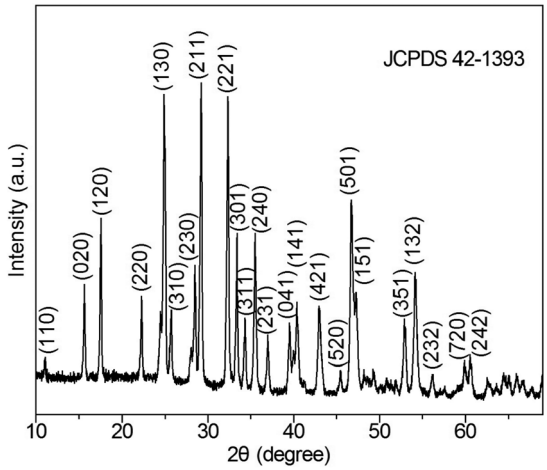


**Fig. 1** XRD pattern of the as-prepared $Sb_2S_3$ product.

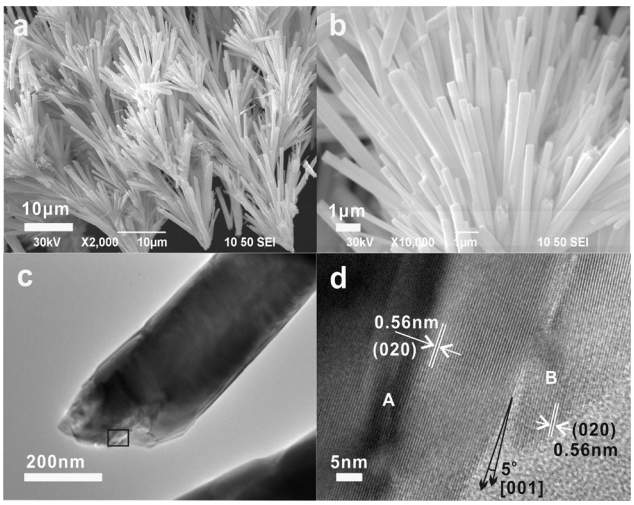


**Fig. 2** SEM images (a, b), TEM image (c) and HRTEM image (d) of the product synthesized at 160 °C for 12 h.

parallel to the side wall throughout the rod reveal the single crystalline nature of the prism. The lattice spacing is estimated to be 0.56 nm, which corresponds to the (020) facets of orthorhombic phase $Sb_2S_3$; this suggests that the longitudinal axis of the rod is along the lattice fringes, *i.e.* along the [001] crystallographic orientation, and the exposed facets of the prism are mainly (020) and (200) facets that are parallel to the [001] orientation, which is the typical structure of 1-dimensional orthorhombic phased $Sb_2S_3$. Detailed observation reveals that a crack presents at the tip of the prism, the separated region A and region B exhibit the same inter-fringe spacing which takes up an angle of ~5°; this directly evidences the crystal splitting from the tip of the prism, implying that the primary rods in $Sb_2S_3$ dendrites are formed by gradual splitting from a larger matrix, which is a universal mode during the crystallization and evolution of $Sb_2S_3$. The structure of an orthorhombic $Sb_2S_3$ crystal is composed of $(Sb_4S_6)_n$ chains parallelly arranged along the [001] direction; the weak van der Waals interactions between the chains lead to ready cleavage of the crystal along the [001] direction,[1] creating 1-dimensional units.

### Influence of reaction conditions

To clarify the effect of PAA on the formation of $Sb_2S_3$ dendrites, the products were also synthesized by merely varying the dosage of PAA. It can be observed from Fig. 3a that the product synthesized without PAA contains non-uniform rods with a diameter of 1–2 μm and a length of about 10 μm, some of them slightly aggregated (Fig. 3a). When 0.05 mL PAA was used in the synthesis process, the product exhibits side by side aggregated rods with a length over 30 μm and diameter up to 5 μm; this suggests that PAA favors the aggregation of $Sb_2S_3$ rods (Fig. 3b). The increase of PAA dosage to 0.1 mL affords larger inhomogeneous rods, which are clearly stacked rods; this suggests that more PAA facilitate more tight aggregation of rods, some dendrites are formed at the tip of the rods, suggesting that the formation of dendrites is also related to PAA (Fig. 3c). Xie *et al.* proposed that $H^+$ is the main species responsible for the tip splitting during the crystallization process;[9e] the acidic PAA herein plays a similar role by etching the surface of $Sb_2S_3$ and therefore accelerates the crystal splitting toward dendrites. When the PAA dosage was increased to 0.5 mL, the product is composed of dendrites with fully split branches (Fig. 3d), highlighting the role of PAA in the formation of $Sb_2S_3$ dendrites. However, a further increase in PAA dosage suppressed the splitting of $Sb_2S_3$ rods, as shown in Fig. 3e, the content of branches decreased apparently when

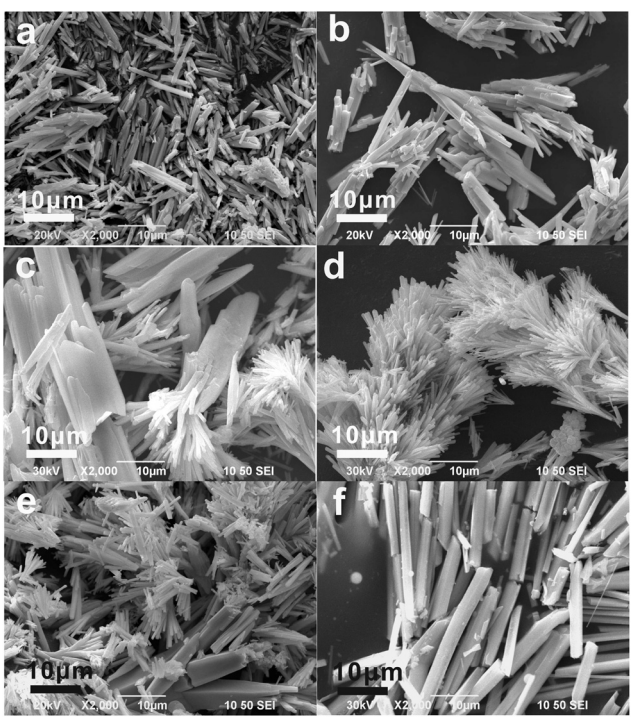


**Fig. 3** SEM images of the products synthesized with different PAA dosages: (a) 0 mL, (b) 0.05 mL, (c) 0.1 mL, (d) 0.5 mL, (e) 2 mL, (f) 3 mL.

2 mL PAA was used, the product is composed of dendrites and rods. When PAA dosage was increased to 3 mL (Fig. 3f), the product shows well-defined rods with a uniform diameter of 3 μm and a length of 15–30 μm; no dendrites can be discerned. Based on these results, it is clear that the PAA dosage is a key factor determining the morphology of $Sb_2S_3$ product. In the solvothermal system, it is supposed that PAA plays dual roles in promoting the aggregation of $Sb_2S_3$ rods and accelerating the crystal splitting. The carboxyl groups on PAA chains are adsorbed on the lateral surface such as (002) or (020) facets of adjacent $Sb_2S_3$ rods; thus drags the rods closer and then aggregate together side by side to form larger rods. Meanwhile, the acidic carboxyl groups on PAA chains can etch the tip of rods, accelerating the crystal splitting toward dendrites. The optimal PAA dosage (0.5 mL) facilitates the full splitting of rods and results in the dendrites. Too high PAA dosage will cause sufficient binding or winding of PAA chains around $Sb_2S_3$ rods, restraining the crystal splitting toward rods. In this sense, the PAA dosage should be well controlled.

The influence of solvothermal temperature on the morphology and phase of $Sb_2S_3$ was also investigated. When the solvothermal reaction was performed at 100 °C, red colored hierarchical microspheres accumulated by primary nanospheres were formed (Fig. 4a), and the phase of the product is amorphous (Fig. 4f), indicating that the temperature is too low to crystallize $Sb_2S_3$. The elevation of temperature to 120 °C afforded a dark red product with a similar morphology but a larger diameter (Fig. 4b); the appearance of a diffraction peak indicates the partial crystallization of the product. When the reaction proceeded at 140 °C, the black product included hierarchical spheres and aggregated $Sb_2S_3$ rods (Fig. 4c); the crystallinity was further increased, indicating that the full conversion of microspheres to rods can only proceed at temperatures over 140 °C. When the temperature was increased up to 160 °C, pure dendrites with high crystallinity were formed (Fig. 4d), indicating the thorough formation of $Sb_2S_3$ dendrites. However, further elevating the temperature to 180 °C, only irregular $Sb_2S_3$ rods with a high crystallinity were obtained (Fig. 4e); no dendrites are discernable. The reason for this phenomenon is unclear, but it at least indicates that too high a temperature is adverse to the formation of $Sb_2S_3$ dendrites. From these results, 160 °C is the optimal temperature toward $Sb_2S_3$ dendrites.

## Formation mechanism

To elucidate the detailed formation mechanism of the crystallized $Sb_2S_3$ dendrites; the products sampled at different stages during the solvothermal reaction were analyzed by SEM and XRD analysis. At a very early stage (10 min), uniform hierarchical microspheres composed of nanospheres were formed (Fig. 5a), and the product is amorphous; this indicates that plenty of $Sb_2S_3$ nanospheres were produced rapidly at the solvothermal temperature; the metastable nanospheres with high surface free energy tend to aggregate to form thermodynamically more stable amorphous microspheres. Prolonging the reaction time (0.5 h) resulted in an increased microsphere diameter and gradual dissolution or etching of the microspheres. From Fig. 5b, partial regions of the microspheres were etched and a faint outline of rods was discerned, the pores between nanospheres gradually disappeared, indicating the slow crystallization of the microspheres. The amorphous phase (Fig. 5i) indicates that the crystallinity of the product is still very low. From the product collected at 1 h, a dense and anisotropic

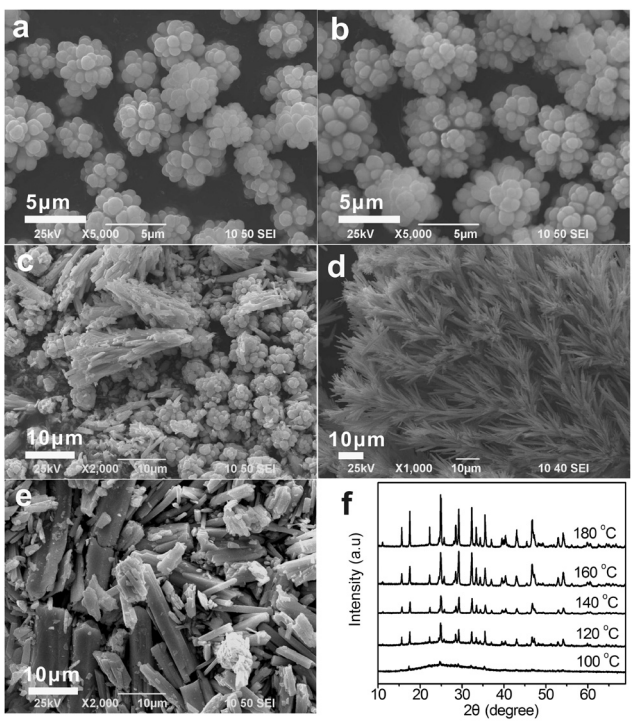


**Fig. 4** SEM images of the $Sb_2S_3$ products prepared at (a) 100 °C, (b) 120 °C, (c) 140 °C, (d) 160 °C, and (e) 180 °C for 12 h; (f) XRD patterns of the products synthesized at different temperatures.

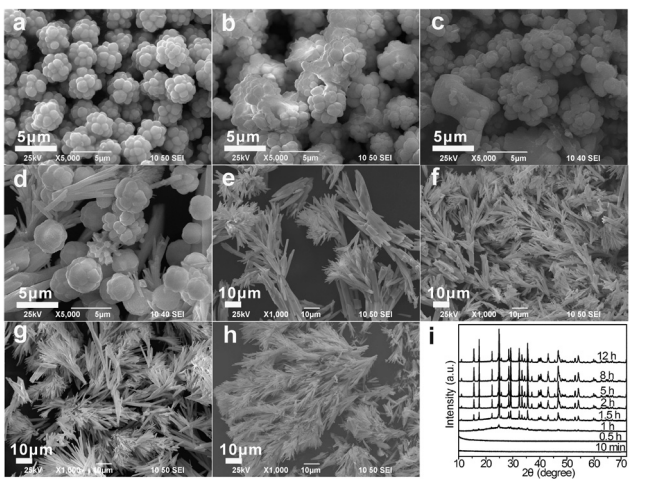


**Fig. 5** SEM images of $Sb_2S_3$ products collected at different reaction times: (a) 10 min, (b) 0.5 h, (c) 1 h, (d) 1.5 h, (e) 2 h, (f) 5 h, (g) 8 h, (h) 12 h. (i) XRD patterns of the products at different reaction times.

short rod covered with ill-defined nanospheres was observed (Fig. 5c); the rod seems to be formed by the dissolution of the nanospheres. The appearance of weak diffraction peaks evidences the elevated crystallinity of the product (Fig. 5i). This suggests that the crystallization and formation of rods proceed at the expense of amorphous microspheres; the etch and dissolution of the microspheres produce oversaturated $Sb_2S_3$, which nucleates at certain region of the microspheres and assembles in the form of $(Sb_4S_6)_n$ chains to afford a thermodynamically favorable crystal with an enhanced aspect ratio, which is a typical Ostwald ripening and crystallization growth process. This phenomenon is more obvious with a prolonged solvothermal time. As shown in Fig. 5d, the product collected at 1.5 h mainly includes side by side aggregated rods (some of them split into several branches) and smooth microspheres with smaller size. According to Ostwald ripening principle, the smaller curvature radius of primary nanospheres is more readily dissolved from the thermodynamic viewpoint, so it is dissolved and results in the crystallization and growth of rods, which are confirmed by the enhanced diffraction peaks shown in Fig. 5i; meanwhile, the microspheres become smooth and the size decreases. When the reaction proceeded for 2 h, only 1-dimensional rod shaped aggregates with high crystallinity were observed (Fig. 5e), confirming that the microspheres were exhausted; some rods split from the tip to form dendrites, indicating that once crystallized $Sb_2S_3$ rods were formed; they started to split; the crystallization and splitting proceeded almost simultaneously. Further prolonging the solvothermal reaction to 5–12 h, it could be observed that the crystal splitting of rods continued and dendrites containing plenty of 1-dimensional branches were gradually formed (Fig. 5f–h).

According to the time dependent experiments, it is supposed that the formation of $Sb_2S_3$ dendrites experiences three stages (Scheme 1); at the first stage (less than 0.5 h), the precipitate reaction produces numerous nanospheres, which accumulate together to form hierarchical amorphous microspheres red in color. The subsequent Ostwald ripening and crystallization processes result in the dissolution of thermodynamic metastable microspheres toward aggregated rods, and the subsequent crystal splitting of the rods affords the $Sb_2S_3$ dendrites composed of 1-dimensional units, which can be intuitively observed from the color evolution of the products to black.

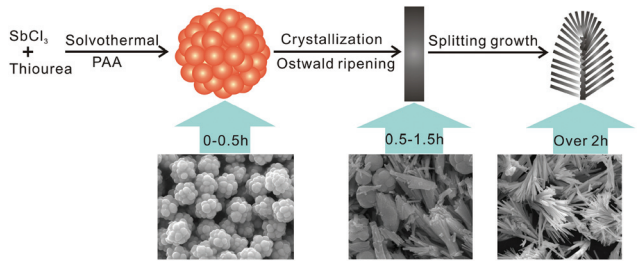


**Scheme 1** Schematic diagram on the formation mechanism of $Sb_2S_3$ dendrites.

## Electrochemical performance

The alterable valence of antimony(III) in $Sb_2S_3$ is an essential feature that can be utilized as a catalyst. Moreover, the high crystallinity and 1-dimensional structure of the primary unit in $Sb_2S_3$ dendrites are also useful for charge transportation. Therefore the $Sb_2S_3$ dendrites can be a potential electrocatalyst in electrochemical detection of electroactive species. Herein, DA was selected as the target molecule to examine the electrochemical activity of $Sb_2S_3$ dendrite. CV curves of 0.1 mM DA dissolved in pH 6.0 PBS at different GCEs as shown in Fig. 6a. It can be seen that CV of DA at bare GCE demonstrated a pair of redox peaks with a 90 mV peak separation and an anodic current of 4.8 μA (curve a). Compared with the bare GCE, the redox potentials at $Sb_2S_3$ dendrite modified GCE were almost unchanged, whereas the response current was enhanced dramatically to 11.7 μA, which is 2.4 times higher than that at bare GCE, indicating the high catalytic activity on the electrochemical oxidation of DA.

The effect of scan rate on the redox currents of DA at the $Sb_2S_3$ dendrites modified GCE is shown in Fig. 6b, It can be observed that the redox peak currents both increased at higher scan rate, and the response current was linearly proportional to the square root of the scan rate in the range of 20–500 mV $s^{-1}$. The relationship between anodic current ($I_{pa}$) and scan rate strictly follows the equation $I_{pa}$ (μA) = 1.7272 $\nu^{0.5}$ − 3.7389 ($r$ = 0.995). This indicates that the electrochemical reactions of

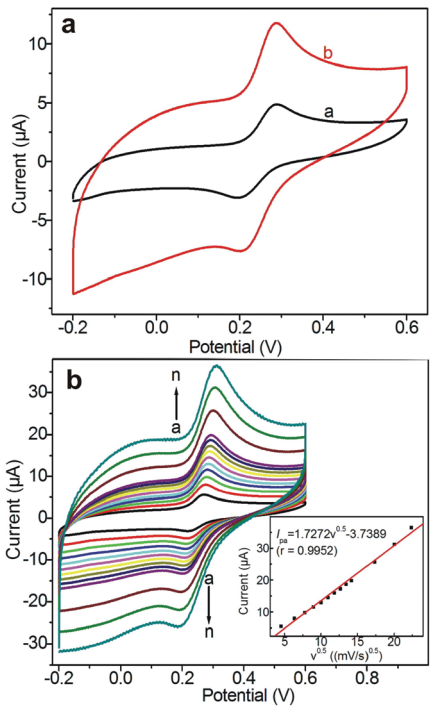


**Fig. 6** (a) CVs of 0.1 mM DA at bare GCE (curve a) and $Sb_2S_3$ dendrites modified GCE (curve b) in 0.1 M PBS (pH 6.0) with a scan rate of 50 mV $s^{-1}$; (b) CVs of 0.1 mM DA in pH 6.0 PBS with scan rates of: 20, 40, 60, 80, 100, 120, 140, 160, 180, 200, 300, 400, and 500 mV $s^{-1}$ (curve a–n). Inset: the plot of peak currents *vs.* square root of scan rates.

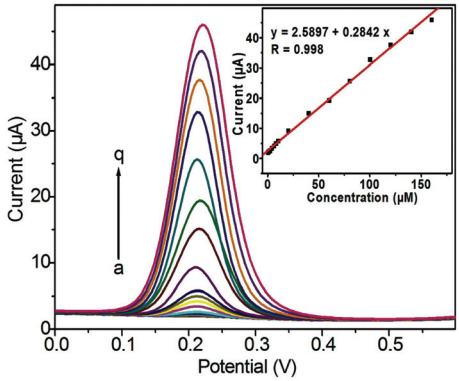


**Fig. 7** DPVs of anodic current with a DA concentration of 0.125, 0.25, 0.5, 1, 2, 4, 6, 8, 10, 20, 40, 60, 80, 100, 120, 140 and 160 μm (from a to q, pH 6.0) at $Sb_2S_3$ dendrites modified GCE with a scan rate of 50 mV $s^{-1}$; inset: plot of peak currents *vs.* DA concentrations.

DA at $Sb_2S_3$ dendrites modified GCE are controlled by the diffusion process.

DPV is a sensitive means to detect the electrochemical response of electroactive species. Fig. 7 shows the DPV curves at $Sb_2S_3$ dendrites modified GCE with different DA concentrations. A series of sharp anodic peaks were observed and the peak currents were elevated linearly with an increase of DA concentrations in the range 0.125–160 μM. The detection limit for DA is estimated to be 0.1 μM at a signal-to-noise ratio of 3. This value is lower than that of $Ag/Ag_2S$ based sensors (1 μM),[17] whereas it is the same as that of a carbon nanotubes–$In_2S_3$ composite based sensor (0.1 μM).[15a]

AA is a commonly concomitant species in actual DA containing specimens. To evaluate the selectivity of $Sb_2S_3$ dendrites modified GCE for DA detection, CV curves of PBS containing 0.1 mM AA, 0.1 mM DA and 0.1 mM DA + 0.1 mM AA were compared. As shown in Fig. 8, no detectable redox peaks were observed for AA (curve a), indicating the inertness of $Sb_2S_3$ dendrites in electrocatalytic oxidation of AA, which is in sharp contrast to that for DA (curve b). The anodic current of 0.1 mM DA + 0.1 mM AA (curve c) is only 8% higher than that of DA alone; the interference is mainly derived from the background of AA, which only brought about a slight interference on electrochemical DA detection. These results indicate that the $Sb_2S_3$ dendrites can be used to selectively detect DA in the presence of AA.

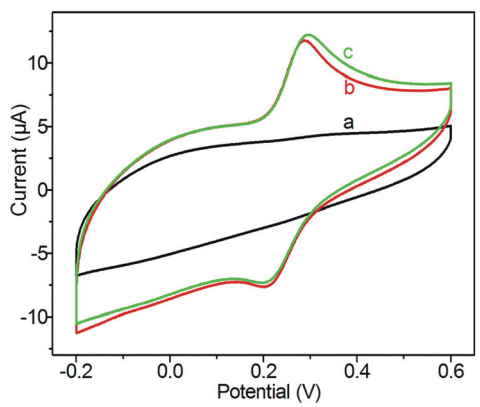


**Fig. 8** CVs of pH 6.0 PBS containing 0.1 mM AA (curve a), 0.1 mM DA (curve b) and 0.1 mM DA + 0.1 mM AA (curve c) at $Sb_2S_3$ dendrites modified GCE with a scan rate of 50 mV $s^{-1}$.

The reproducibility of the $Sb_2S_3$ dendrites modified GCE was also evaluated by CV measurements of 0.1 mM DA at five parallel modified GCEs; 3.7% relative standard deviation (RSD) of anodic currents approves the good fabrication reproducibility of the sensor. The anodic response currents at a certain electrode decreased by 4.1% after five cycles of CV measurements with an interval of 20 min, the acceptable stability may be due to the high structural stability of $Sb_2S_3$ dendrites. Over 91% of anodic current remained from CV after the $Sb_2S_3$ dendrites modified GCE was stored at room temperature for a week, suggesting the basically acceptable long term reliability. These results indicate that the $Sb_2S_3$ dendrites can be an acceptable sensing material for electrochemical DA detection.

## Conclusions

In summary, $Sb_2S_3$ dendrites were synthesized by a facile solvothermal reaction; the dosage of PAA and the reaction temperature are essential for the formation of the product. Temporal experiments suggest that the amorphous microsphere formation, Ostwald ripening and crystallization, as well as the crystal splitting process converged in promoting the formation of $Sb_2S_3$ dendrites containing 1-dimensional units. The product can be used as a potential sensing material for electrochemical detection of DA with a low detection limit and good selectivity against AA.

## Acknowledgements

This work was supported by the National Science Foundation of China (no. 61204078 and 61176004), Program for Innovative Research Team (in Science and Technology) in University of Henan Province (No. 13IRTSTHN026), the Science and Technology Breakthrough Project of Henan Province (no. 122102210561) and the Key Project of Science and Technology of Xinxiang City.

## Notes and references

1 (*a*) G. Y. Chen, B. Dneg, G. B. Cai, T. K. Zhang, W. F. Dong, W. X. Zhang and A. W. Xu, *J. Phys. Chem. C*, 2008, **112**, 672; (*b*) G. Y. Chen, W. X. Zhang and A. W. Xu, *Mater. Chem. Phys.*, 2010, **123**, 236.

2 (*a*) H. Wedemeyer, J. Michels, R. Chmielowski, S. Bourdais, T. Muto, M. Sugiura, G. Dennler and J. Bachmann, *Energy Environ. Sci.*, 2013, **6**, 67; (*b*) F. T. F. O'Mahony, T. Lutz, N. Guijarro, R. Gomez and S. A. Haque, *Energy Environ. Sci.*, 2012, **5**, 9760; (*c*) J. C. Cardoso, C. A. Grimes, X. J. Feng, X. Y. Zhang, S. Komarneni, M. V. B. Zanonid and

 

N. Z. Bao, *Chem. Commun.*, 2012, **48**, 2818; (*d*) D. B. Salunkhe, S. S. Gargote, D. P. Dubal, W. B. Kim and B. R. Sankapal, *Chem. Phys. Lett.*, 2012, **554**, 150.

3 (*a*) M. Sun, D. Z. Li, W. J. Li, Y. B. Chen, Z. X. Chen, Y. H. He and X. Z. Fu, *J. Phys. Chem. C*, 2008, **112**, 18076; (*b*) X. M. Shuai and W. Z. Shen, *Nanoscale Res. Lett.*, 2012, **7**, 199; (*c*) W. G. Tao, J. L. Chang, D. P. Wu, Z. Y. Gao, X. L. Duan, F. Xu and K. Jiang, *Mater. Res. Bull.*, 2013, **48**, 538.

4 (*a*) F. Cao, W. Q. Liu, L. Zhou, R. P. Deng, S. Y. Song, S. Wang, S. Q. Su and H. J. Zhang, *Solid State Sci.*, 2011, **13**, 1226; (*b*) J. M. Ma, X. C. Duan, J. B. Lian, T. Kim, P. Peng, X. D. Liu, Z. F. Liu, H. B. Li and W. J. Zheng, *Chem.–Eur. J.*, 2010, **16**, 13210; (*c*) C. M. Park, Y. Hwa, N. E. Sung and H. J. Sohn, *J. Mater. Chem.*, 2010, **20**, 1097; (*d*) H. M. Yang, X. H. Su and A. D. Tang, *Mater. Res. Bull.*, 2007, **42**, 1357.

5 H. F. Bao, X. Q. Cui, C. M. Li, Q. L. Song, Z. S. Lu and J. Guo, *J. Phys. Chem. C*, 2007, **111**, 17131.

6 J. Varghese, S. Barth, L. Keeney, R. W. Whatmore and J. D. Holmes, *Nano Lett.*, 2012, **12**, 868.

7 Q. F. Han, Y. W. Yuan, X. H. Liu, X. D. Wu, F. L. Bei, X. Wang and K. J. Xu, *Langmuir*, 2012, **28**, 6726.

8 (*a*) W. J. Lou, M. Chen, X. B. Wang and W. M. Liu, *Chem. Mater.*, 2007, **19**, 872; (*b*) H. M. Hu, M. S. Mo, B. J. Yang, X. J. Zhang, Q. W. Li, W. C. Yu and Y. T. Qian, *J. Cryst. Growth*, 2003, **258**, 106.

9 (*a*) Q. F. Han, J. Lu, X. J. Yang, L. D. Lu and X. Wang, *Cryst. Growth Des.*, 2008, **8**, 395; (*b*) H. M. Hu, Z. P. Liu, B. J. Yang, M. S. Mo, Q. W. Li, W. C. Yu and Y. T. Qian, *J. Cryst. Growth*, 2004, **262**, 375; (*c*) C. Pilaponga, T. Thongtema and S. Thongtem, *J. Alloys Compd.*, 2010, **507**, L38; (*d*) I. L. Validzic, N. D. Abazovic, S. P. Ahrenkiel and I. A. Jankovic, *J. Cryst. Growth*, 2012, **354**, 157; (*e*) X. B. Cao, Y. Xie and L. Y. Li, *J. Solid State Chem.*, 2004, **177**, 202.

10 (*a*) A. A. Ensafi, M. Taei and T. Khayamian, *J. Electroanal. Chem.*, 2009, **633**, 212; (*b*) S. R. Hou, N. Zheng, H. Y. Feng, X. J. Li and Z. B. Yuan, *Anal. Biochem.*, 2008, **179**, 179.

11 R. M. Wightman, L. J. May and A. C. Michael, *Anal. Chem.*, 1988, **60**, 769A.

12 (*a*) M. R. Moghadam, S. Dadfarnia, A. M. H. Shabani and P. Shahbazikhah, *Anal. Biochem.*, 2011, **410**, 289; (*b*) H. Zhao, H. Mu, Y. Bai, H. Yu and Y. Hu, *J. Pharm. Anal.*, 2011, **1**, 208; (*c*) R. R. González, R. F. Fernández, J. L. M. Vidal, A. G. Frenich and M. L. G. Pérez, *J. Neurosci. Meth.*, 2011, **198**, 187.

13 (*a*) M. Hadi and A. Rouhollahi, *Anal. Chim. Acta*, 2012, **721**, 55; (*b*) X. Zhu, Q. Liu, X. H. Zhu, C. L. Li, M. T. Xu and Y. Liang, *Int. J. Electrochem. Sci.*, 2012, **7**, 5172; (*c*) Z. H. Sheng, X. Q. Zheng, J. Y. Xu, W. J. Bao, F. B. Wang and X. H. Xia, *Biosens. Bioelectron.*, 2012, **34**, 125.

14 S. Reddya, B. E. K. Swamya and H. Jayadevappa, *Electrochim. Acta*, 2012, **61**, 78.

15 (*a*) Z. J. Yang, X. C. Huang, J. Li, Y. C. Zhang, S. H. Yu, Q. Xu and X. Y. Hu, *Microchim. Acta*, 2012, **177**, 381; (*b*) J. Li, J. Yang, Z. J. Yang, Y. F. Li, S. H. Yu, Q. Xu and X. Y. Hu, *Anal. Methods*, 2012, **4**, 1725; (*c*) S. Liu, J. Yan, G. W. He, D. D. Zhong, J. X. Chen, L. Y. Shi, X. M. Zhou and H. J. Jiang, *J. Electroanal. Chem.*, 2012, **672**, 40; (*d*) L. Wu, L. Y. Feng, J. S. Ren and X. G. Qu, *Biosens. Bioelectron.*, 2012, **34**, 57; (*e*) M. P. Ngoc Bui, C. A. Li and G. H. Seong, *Biochip J.*, 2012, **6**, 149; (*f*) Y. Y. Li, J. Du, J. D. Yang, D. Liu and X. Q. Lu, *Colloids Surf., B*, 2012, **97**, 32.

16 I. D. O. Matos and W. A. Alves, *ACS Appl. Mater. Inter.*, 2011, **3**, 4437.

17 C. Yan Li, Y. J. Cai, C. H. Yang, C. H. Wu, Y. Wei, T. C. Wen, T. L. Wang, Y. T. Shieh, W. C. Lin and W. J. Chen, *Electrochim. Acta*, 2011, **56**, 1955.